Research Article Vol. 13, No. 4 / 1 Apr 2022 / Biomedical Optics Express 2068
Biomedical Optics EXPRESS

Speckle-resolved optical coherence tomography for mesoscopic imaging within scattering media

MICHELLE CUA,[1,2] BAPTISTE BLOCHET,[1] AND CHANGHUEI YANG[1,3]

[1]Department of Electrical Engineering, California Institute of Technology, 1200 E. California Blvd, Pasadena, CA 91152, USA
[2]ecua@caltech.edu
[3]chyang@caltech.edu

Abstract: Light scattering poses a challenge for imaging deep in scattering media as the ballistic light exponentially attenuates with depth. In contrast to the ballistic light, the multiply scattered light penetrates deeper and also contains information about the sample. One technique to image deeper is to selectively detect only a subset of the multiply scattered light, namely the 'snake' photons, which are predominantly forward scattered and retain more direct information than the more strongly scattered light. In this work, we develop a technique, termed speckle-resolved optical coherence tomography (srOCT), for efficiently detecting these 'snake' photons to enable imaging deeper in scattering media. The system couples spatio-angular filtering with speckle-resolved interferometric detection to preferentially and efficiently detect the weakly scattered 'snake' photons. With our proof-of-concept system, we demonstrate depth-resolved imaging beyond the ballistic limit, up to a depth of 90 round-trip MFPs in a scattering phantom and a depth of 4.5 mm of chicken tissue at 0.4 mm axial and lateral resolution.

1. Introduction

Light scattering poses a challenge for optical imaging through turbid media as it degrades image quality and enforces a trade-off between resolution and penetration depth. Ballistic imaging methods, such as confocal microscopy and Optical Coherence Tomography (OCT), aim to detect the singly-back-scattered, ballistic light through the use of gating methods such as time gating, polarization gating, and confocal gating [1]. A newer technique, CASS (collective accumulation of single scattering) microscopy, uses time-gated detection and correlations in the input-output response in order to preferentially detect singly-scattered light [2]. Although these methods provide at- or near- diffraction-limited resolution, they are limited in penetration depth due to two factors: (1) the ballistic light attenuates exponentially with depth, and (2) the multiply-scattered light becomes increasing challenging to reject [3,4]. The limit is approximately 23 round-trip mean free paths (MFPs) for CASS and 27 MFPs for OCT [2,5,6].

In contrast, if diffraction-limited resolution is not required, then one can image deeper by utilizing the scattered light. Methods such as laminar optical tomography (LOT) and diffuse optical tomography (DOT) detect the scattered light [7–9]. These methods are feasible since scattering is dominant over absorption at optical wavelengths in biological tissues. LOT achieves resolutions on the order of hundreds of micrometers at depths of a few millimeters in tissue [9]. DOT, on the other hand, works in the diffusive regime and is able to image objects buried centimeters underneath tissue at resolutions approaching 20% of the imaging depth [10]. However, these methods require characterization of the scattering properties and/or computational techniques in order to 'invert' the scattering process and retrieve information about the object.

Another strategy to image deeper is to acquire only a subset of the scattered light. The scattered light can be loosely categorized into two groups: (1) weakly-scattered 'snake' photons that are predominantly forward scattered and (2) more-strongly-scattered 'diffuse' photons. Preferential selection of the 'snake' photons over the more-strongly-scattered 'diffuse' photons can allow for

#448969 https://doi.org/10.1364/BOE.448969
Journal © 2022 Received 1 Dec 2021; revised 5 Feb 2022; accepted 6 Feb 2022; published 14 Mar 2022

Biomedical Optics EXPRESS

imaging past the ballistic limit at moderate resolution in a direct fashion [11–13]. Early works demonstrated that detecting only the least scattered light improved resolution in trans-illumination imaging schemes [14–16]. More recently, the multiple-scattering, low-coherence interferometric (ms/LCI) systems utilized this concept to surpass the ballistic limit and perform epi-illumination imaging deep within scattering media, up to 40 round-trip mean free paths (MFPs) in a $g = 0.95$ sample and 90 MFPs in a $g = 0.988$ sample [13,17,18]. The msLCI systems employed a narrow collection aperture as well as offset illumination and detection to preferentially detect snake photons. These systems also required either long acquisition times or the incoherent averaging of many signals, up to 10^6 signals, to boost the signal-to-noise ratio [13,17,19].

In this work, we present Speckle-Resolved OCT (srOCT), a system that employs spatio-angular filtering in conjunction with speckle-resolved detection to preferentially detect the weakly scattered light in an efficient manner. We investigate whether spatial or angular filtering is more effective at preserving imaging resolution. We also demonstrate that speckle-resolved detection is an efficient method as it allows one to perform incoherent averaging in a single-shot manner. With this proof-of-concept system, we perform depth-resolved imaging beyond the ballistic limit, to a depth of 90 MFPs in a $g = 0.96$ scattering phantoms and a depth of 4.5 mm in chicken breast tissue at 0.4 mm axial and lateral resolution.

2. Simulation

Figure 1 depicts one of the concepts behind Speckle-Resolved OCT (srOCT). The back-scattered light from the sample can be separated into two categories: (1) the weakly scattered "snake" photons (in blue) that are predominantly forward scattered and contain information about the target, and (2) the strongly scattered "diffuse" photons (in purple) that degrade contrast and resolution [12,13]. The goal of srOCT is to preferentially detect the weakly scattered photons in an efficient manner. If snake photons exit the tissue at a closer distance to the incident light position or at narrower angles, then filtering the photons based on their exit position and/or angle may aid in preferentially detecting these snake photons, which translates to better imaging resolution. In this work, we investigate the impact that spatio-angular filtering (Fig. 1(b)) has on the imaging resolution and show that filtering provides an enhancement in lateral and axial resolution (Fig. 1(c)).

We first investigated whether spatial and/or angular filtering improves resolution using Monte Carlo simulations. Simulations were performed with a pencil beam incident on to the center of a homogeneous scattering slab ($\mu_s = 10\text{mm}^{-1}, g = 0.90$) that was 500x500x500 mm^3 (MCX [20]). A scattering anisotropy of $g = 0.90$ was chosen as this is a typical, representative value for biological tissue [10]. A total of 10^9 photons were simulated. Specular reflections from the tissue and air interface were ignored. Photons that exited the top surface of the slab, up to a distance of 100 mm from the center of the slab, were detected. For each photon, the following parameters were quantified: (1) s, the pathlength travelled in tissue; (2) $x_{\text{max}}, y_{\text{max}}, z_{\text{max}}$, the position of the photon at the maximum depth it travelled; (3) r, the exit position, measured as the distance from the incident light position; and (4) θ, the exit angle, measured relative to the angle for ballistic light detection, which is normal to the surface. For a target located at depth z_{depth}, only a subset of photons that interacted with the target, defined as $z_{\text{max}} \in [z_{\text{targ}} - \Delta z, z_{\text{targ}} + \Delta z]$, were considered detected. Some of these parameters have been shown in Fig. 2(b).

To measure the impact of spatio-angular filtering on improving lateral and axial resolution, the detected photons were filtered based on their exit position r and exit angle θ such that only those that satisfied $r \leq r_{\text{thr}}, \theta \leq \theta_{\text{thr}}$ were included, for some spatial range r_{thr} and angular range θ_{thr} (Fig. 2(a)). The lateral and axial resolutions were estimated from the distribution in their position at maximum depth $x_{\text{max}}, y_{\text{max}}$ and apparent depth $z_{\text{depth}} = \frac{s}{2n_{med}}$, respectively. The lateral resolution was estimated from the variance of $x_{\text{max}}, y_{\text{max}}$, which were considered to have the same underlying distribution due to symmetry (Fig. 2(c)). The axial resolution was estimated

Biomedical Optics EXPRESS

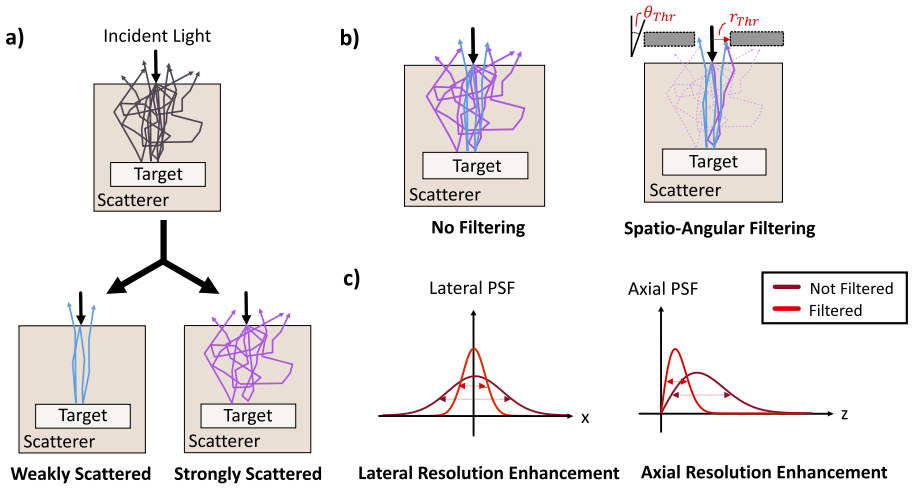

Fig. 1. Speckle-Resolved OCT Concept. a) Two types of back-scattered photons are considered: (1) non-scattered and weakly-scattered 'snake' photons (in blue) that are predominantly forward scattered and contain information about the structure of the target, and (2) strongly-scattered 'diffuse' photons (in purple) that degrade contrast and resolution. b) Filtering the back-scattered photons by their exit position and/or exit angle preferentially rejects diffuse photons. c) Spatio-angular filtering enhances the lateral and axial resolution.

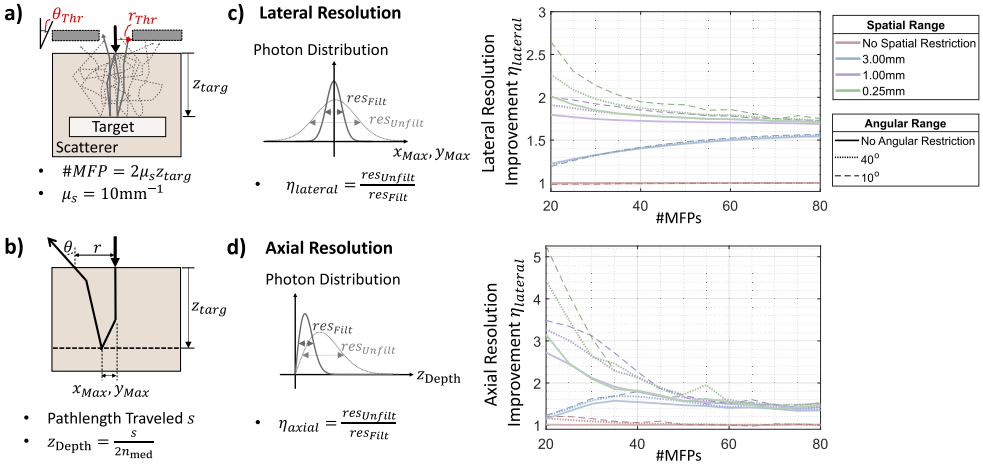

Fig. 2. Impact of Spatial and Angular Restriction on Resolution. a) Spatio-angular filtering restricts the detected photons to those that satisfy $r \leq r_{\text{thr}}, \theta \leq \theta_{\text{thr}}$, for a given target located at depth z_{targ}, $\#MFPs = \mu_S z_{targ}$. b) Parameters measured include the exit position r, exit angle θ, lateral position at the target $x_{\text{max}}, y_{\text{max}}$, and pathlength travelled s. c), d) Impact of spatial restriction (in different colors) and/or angular restriction (in different linetypes) on improving the lateral and axial resolution. The enhancement is computed relative to the unfiltered case. Restricting the spatial range improves the resolution. Angular restriction improves resolution when combined with spatial filtering.

by measuring the full-width-at-half-maximum (FWHM) of the distribution of apparent depth $z_{\text{depth}} = \frac{s}{2n_{\text{med}}}$ (Fig. 2(d)).

Figure 2(c,d) provides a plot showing the improvement in lateral and axial resolution with spatio-angular filtering, for spatial and angular restrictions of $r_{\text{thr}} \in [0.25\text{mm}, 100\text{mm}]$ and

Biomedical Optics EXPRESS

$\theta_{\text{thr}} \in [10\,\text{deg}, 90\,\text{deg}]$. The resolution improvement was defined relative to the resolution for the unfiltered case. To normalize the depth of imaging in scattering media with various scattering strengths, the target depth was reported as the number of round-trip mean free paths (#MFPs), which was defined as #MFPs $= 2\mu_s z_{\text{depth}}$ where μ_s is the scattering coefficient.

For both lateral and axial resolution, spatial restriction improved the resolution to about 2 to 3 times for all depths studied. In the absence of any spatial restriction, angular restriction did not seem to improve resolution. However, angular restriction in conjunction with spatial restriction provides a further improve, with more impact at shallower depths. Therefore, a combination of both spatial and angular filtering should be employed to maintain resolution.

3. Experimental results

Figure 3 depicts the principle behind how spatio-angular filtering is achieved experimentally. Light is weakly focused on the target. The back-scattered light from the target is detected by a camera. A reference beam, incident at an angle ϕ, interferes with the back-scattered light from the sample. The detected interference image at the camera contains information about the exit position and angle of the back-scattered light, which can be used to exclude some detected photons from processing (shown in gray). From this image, the back-scattered intensity from a given spot in the sample is measured.

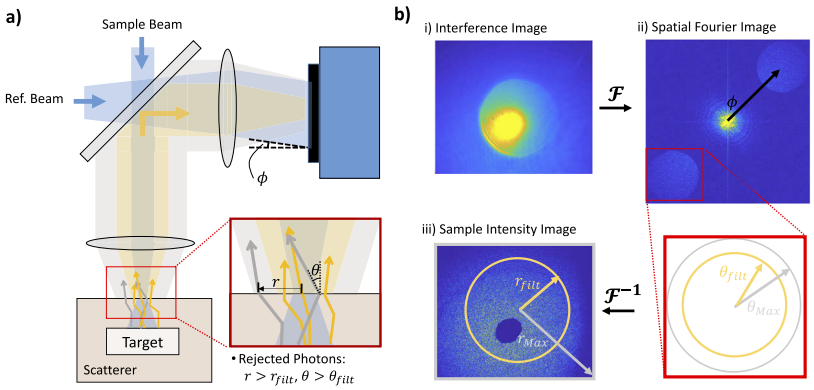

Fig. 3. Principle of Speckle-Resolved OCT (srOCT). a) Light is weakly focused on a target located within a scattering medium. The exit position and angle of the back-scattered photons is used to preferentially reject the more strongly scattered photons (in gray) from the weakly scattered photons (in yellow). b) The filtering of photons based on exit position and angle is accomplished in processing. i) The detected interference pattern, which contains information about the intensity of the back-reflected sample light. ii) The spatial Fourier transform of the interference image contains a central peak and two side lobes. The side lobes can be used to limit the processed photons to those that satisfy $\theta \leq \theta_{\text{filt}}$. iii) The inverse Fourier transform of one side lobe provides information of the back-scattered sample light and can be used to spatially filter the processed photons to those that satisfy $r \leq r_{\text{filt}}$.

Although the spatial and angular range is restricted based on the optical setup, further spatio-angular filtering can be performed in post-processing (Fig. 3(b)). Angular filtering is performed in the spatial Fourier domain whereas spatial filtering is performed in the spatial domain. The Spatial Fourier transform of the interference image (in Fig. 3(b),ii) contains a main lobe and two side lobes whose centers are shifted due to the reference angle tilt ϕ. The side lobe contains information about the exit angle of the back-scattered light and can be used to limit the processing only to photons whose exit angles satisfy $\theta \leq \theta_{\text{thr}}$. The inverse Fourier transform of one of the side lobes provides information about the exit position of the scattered light and can be used to

Biomedical Optics EXPRESS

restrict the processing to only include photons whose exit positions satisfy $r \leq r_{\text{thr}}$ (Fig. 3(b),iii). Summing up the power within r_{thr} provides a measure of the sample intensity at a given x, y, z point.

The experimental setup for srOCT is shown in Fig. 4. The system employs a digital off-axis holographic interferometer with a short-coherence light source to measure the intensity of the back-scattered light from a given point in the sample [21–25]. Light from a SLD (SLD830S-A20; $\lambda = 830\text{nm}, \Delta\lambda = 20\text{nm}$; Thorlabs, NJ) was split by a fiber coupler into two arms, with 90% of the light going to the sample arm and 10% of the light going to the reference arm. In the reference arm, light was first collimated by lens f_c and then directed towards a transmission grating (G; 300 grooves/mm, GTI25-03A; Thorlabs, NJ); only the first order of the diffracted beam was expanded and detected by the camera (PCOEdge 5.5; PCO, Germany). The diffracted beam provided the required tilt in the reference beam without adding a pathlength mismatch so that the spatial extent of the interference pattern at the camera would not be limited due to the short temporal coherence of the light source [25–27].

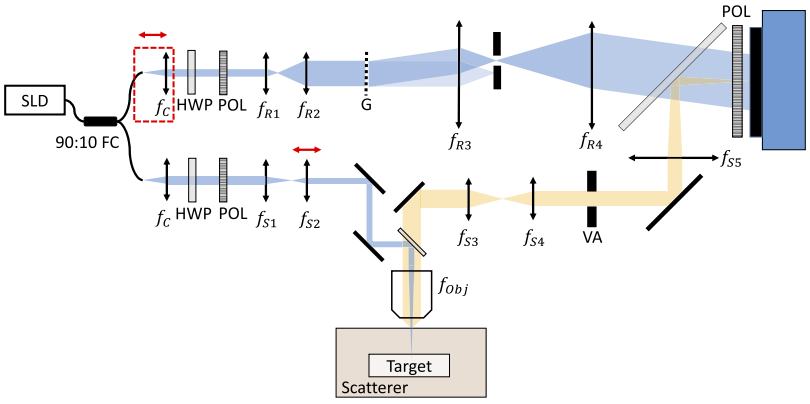

Fig. 4. Experimental Setup for Speckle-Resolved OCT. Light from an SLD is split into two arms, with 10% of the light going to the reference arm (top) and 90% to the sample arm (bottom). The reference beam is collimated and incident upon a transmission grating; only the first order diffracted beam is incident on the camera. The reference arm length is adjusted by moving the components in the red box. The sample beam is incident upon an objective lens, which weakly focuses light on the target. The back-scattered light (in yellow) is transmitted by two 4f imaging systems to the camera, which is conjugated to the surface of the scattering medium. *Abbreviations: FC, fiber coupler; f, lens; G, grating; HWP, half-wave plate; Obj, objective lens; POL, polarizer; and VA, variable aperture. Lens focal lengths:* $f_c = 7.5mm, f_{R1} = 10mm, f_{R2} = 35mm, f_{R3} = 75mm||100mm, f_{R4} = 200mm, f_{S1} = 40mm, f_{S2} = 30mm, f_{Obj} = 12.5mm, f_{S3} = 125mm, f_{S4} = 100mm, f_{S5} = 200mm$.

In the sample arm, light was first collimated and then transmitted to a water-immersion objective lens (N16XLWD-PF; Thorlabs, NJ), which weakly focused the light onto the target. The focus was adjusted by translating lens f_{S2}. The back-scattered light from the sample was transmitted by two 4-f systems to the camera, which was conjugated to the surface of the sample.

The interference pattern between the reference and sample beam was detected by a camera and contained information about the sample intensity from a given x, y, z point. The detected interference image can be mathematically represented as

$$I_{\text{det}}(\mathbf{r}) = |\mathbf{E_R} + \mathbf{E_S}(\mathbf{r})|^2 + I_x(\mathbf{r}) = I_R + I_S(\mathbf{r}) + I_x(\mathbf{r}) + 2E_R E_S(\mathbf{r}) \cos(k_0 \sin(\boldsymbol{\phi}) \cdot \mathbf{r} + \theta_R - \theta_S(\mathbf{r})), \quad (1)$$

where $\mathbf{E_R}, \mathbf{E_S}$ are the complex fields of the reference beam and interfering portion of the sample beam respectively; I_x is the sample intensity of the non-interfering portion; $I_R = |\mathbf{E_R}|^2, I_S = |\mathbf{E_S}|^2$

Biomedical Optics EXPRESS

are the reference and sample intensities; $k_0 = \frac{2\pi}{\lambda}$ is the wavenumber; $\mathbf{r} = (x, y)$ is the lateral position; $\boldsymbol{\phi} = (\phi_x, \phi_y)$ is the reference beam tilt angle; and $\sin(\boldsymbol{\phi}) = (\sin(\phi_x), \sin(\phi_y))$. The reference beam is modelled as a plane wave. The complex speckle field of the sample beam is denoted $\mathbf{E_S}(\mathbf{r}) = E_S(\mathbf{r})e^{j\theta_S(\mathbf{r})}$. For interference, the difference in pathlength between the sample and reference beams must be within the coherence length of the source.

In the spatial Fourier domain, this equation becomes:

$$\tilde{I}_{\text{det}}(\mathbf{k}) = \mathcal{F}\left[I_R + I_S + I_x\right](\mathbf{k}) + \mathcal{F}\left[E_R E_S e^{\pm j(\theta_R - \theta_S)}\right](\mathbf{k} \pm k_0 \sin(\boldsymbol{\phi})), \tag{2}$$

where $\mathcal{F}[\cdot]$ denotes the 2D Fourier transform, $\tilde{I}_{det}(\mathbf{k}) = \mathcal{F}[I_{det}(\mathbf{r})]$, and $\mathbf{k} = (k_x, k_y)$. The two side lobes centered at $\mathbf{k}_{\text{shift}} = \pm k_0 \sin(\boldsymbol{\phi})$ contain information about the sample beam $\mathcal{F}\left[E_R E_S e^{\pm j(\theta_R - \theta_S)}\right]$. The back-scattered information from the sample can be extracted by isolating and computing the inverse Fourier transform of one of the side lobes, which yields $E_R E_S e^{\pm j(\theta_R - \theta_S)}$. A reference-only image provides an estimate of E_R. The back-scattered sample light, $\mathbf{E_S} = E_S e^{j\theta_S}$, forms a characteristic speckle pattern with each speckle grain having a random phase and amplitude. The speckle information is summed incoherently by discarding the phase to estimate the back-scattered light intensity from the sample at a given x, y, z point.

To acquire data, a depth scan, or a-scan, was acquired by imaging the sample at a given lateral position while scanning axially in z. A cross-sectional b-scan, which provides an image of depth vs lateral dimension, was acquired by scanning z as well as either x or y. Axial scanning was performed by adjusting the length of the reference by placing the fiber coupler input and collimating lens f_c on a translation stage. Lateral scanning was achieved by placing the sample on an actuated translated stage (LTA-HS; Newport, CA).

The incident light power on the sample was 0.7 mW, and the system had an axial resolution of 15 µm in PDMS. The lateral resolution of the system varied depending on the thickness of the sample and ranged from 50 µm to 100 µm in PDMS. The interference image was acquired with a camera exposure time of 1 ms to 4 ms. The exposure time was limited by large back-reflections from the back-aperture of the objective lens and the sample, which was orders-of-magnitude larger than the back-reflected scattered light from the sample and saturated the camera detector.

The back-scattered sample light $\mathbf{E_S}$ forms a speckle field with speckle grain size determined by the detection system optics. For speckle-resolved detection, the speckle grain size must satisfy $d_{\text{speckle}} \geq 3.12 d_{\text{pixel}}$ in order to prevent aliasing in the Fourier domain and ensure that each speckle grain is resolved by at least one detector element. The speckle size at the camera is given by $d_{\text{speckle}} = \frac{\lambda}{2}\frac{M}{NA}$ where M is the magnification and NA is the numerical aperture of the detection path [28]. In our case, $M = 20$ and $NA \leq 0.4$, which resulted in a speckle size of $d_{\text{speckle}} \geq 21$ µm. Due to the physical dimensions of the camera along with the detection optics, the maximum spatial and angular range of the setup was $r_{\text{thr,exp}} = 0.35$mm and $\theta_{\text{thr,exp}} = 17.4$ deg and the maximum number of speckles detectable by our system was $4{\times}10^5$ speckles. The maximum spatial range $r_{\text{thr,exp}}$ and angular range $\theta_{\text{thr,exp}}$ of the experimental setup are close to the smallest that was tested in simulation as this provided the best resolution.

3.1. Imaging scattering phantoms

Scattering phantoms were constructed to determine the srOCT system response. These scattering phantoms were fabricated by dispersing polystyrene microspheres (Polysciences, Inc., PA) in polydimethylsiloxane (PDMS; MilliporeSigma, MO). 1 µm and 3 µm beads were used to construct two different phantoms with the following scattering properties: (1) $g = 0.91$, $\mu_S = 11\text{mm}^{-1}$ and (2) $g = 0.96$, $\mu_S = 16\text{mm}^{-1}$ (as determined by Mie theory). A thickness-matched layer of PDMS was also included to aid in alignment.

The scattering phantom was placed on top of a USAF resolution target (Thorlabs, NJ) in order to measure the lateral and axial resolution (Fig. 5(a)). The edges of the square target were

Biomedical Optics EXPRESS

used to measure lateral resolution whereas the axial response to the chrome reflector was used to measure axial resolution. Figure 5(b,c) show cross-sectional b-scans of the edge through various thicknesses of scattering media for both types of samples. The SNR decreases with thicker scattering media; however, the signal from the edge is still clearly seen, even below a 2.77 mm-thick phantom, corresponding to 89 round-trip MFPs.

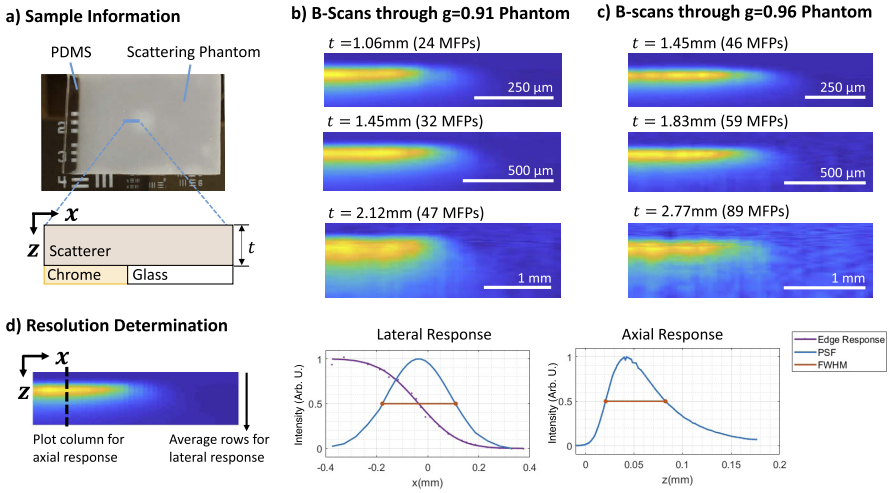

Fig. 5. Imaging through a Scattering Phantom. a) The sample, consisting of a scattering phantom (polystyrene microspheres embedded in PDMS) and a thickness-matched transparent PDMS layer, is placed upon a USAF resolution target. Approximate location of acquired b-scans is shown in blue. b), c) B-scans of the target, acquired through various thicknesses of scattering media t, for phantoms with scattering anisotropy of $g = 0.91$ and $g = 0.96$ respectively. d) The lateral and axial resolution is determined from the b-scan.

Figure 5(d) depicts the process for measuring the lateral and axial resolution. For the axial response, an a-scan was acquired with a chrome target located beneath the scattering phantom. For the lateral response, a b-scan was acquired at the approximate location shown by the dashed line. The rows of the b-scan were averaged to compute the edge response. The integral of a Gaussian curve was fitted to denoise the edge response, and the derivative of this fitted edge response yielded the lateral response. The lateral and axial resolution were estimated by computing the FHWM of the lateral and axial responses, respectively.

Figure 6 shows the lateral and axial resolution as a function of both the number of round-trip MFPs and TMFPs. The resolution has been normalized to the target depth. Both the lateral resolution (Fig. 6(a)) and axial resolution (Fig. 6(c)) worsen with increasing depth. However, the resolution degrades more slowly for scattering media with higher anisotropy. When plotted as a function of TMFPs (Fig. 6(b,d)), the lateral and axial resolutions appear to degrade at a similar rate for both types of scattering phantom.

We also investigated the impact of performing further spatio-angular filtering on the acquired data sets (Fig. 6); the filtered points have been shown as circles. Experimentally, $r_{\text{thr}} \in [10\ \mu\text{m}, 350\ \mu\text{m}], \theta_{\text{thr}} \in [1\,\text{deg}, 17.4\,\text{deg}]$. The results for no further filtering ($r_{\text{thr}} = 350\ \mu\text{m}, \theta_{\text{thr}} = 17.4\,\text{deg}$; shown as x's) have been shown alongside the best results we could measure with further filtering. Filtering improved the lateral resolution by 1.3 ± 0.3x and axial resolution by 1.5 ± 0.5x.

Biomedical Optics EXPRESS

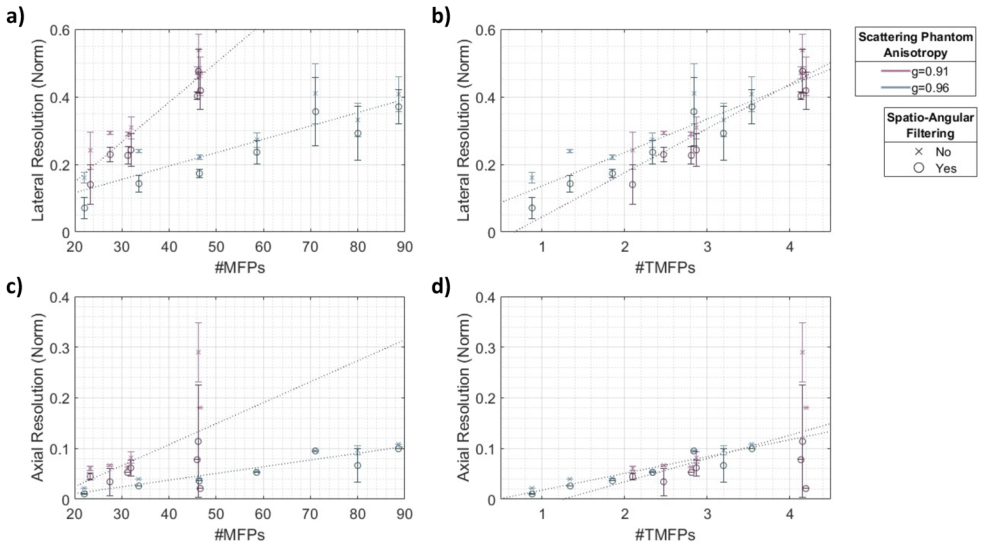

Fig. 6. Lateral and Axial Resolution of srOCT. The lateral and axial resolution of srOCT for a chrome target placed behind various scattering phantoms was determined. The resolution is normalized to the target depth. The lateral and axial resolution are shown as a function of number of round-trip mean free paths (MFPs) (a), c) respectively) and number of round-trip transport mean free paths (TMFPs) (b),d) respectively).

3.2. SNR

Two of the aims of the paper were: (1) to investigate whether spatial or angular filtering impacted imaging resolution, and (2) to introduce speckle-resolved detection as an efficient method for detecting multiply scattered photons. Through simulation, we showed that spatial filtering improves imaging resolution, and angular filtering provides an enhancement only in conjunction with spatial filtering. We now turn our attention to the benefit of speckle-resolved detection.

When imaging in scattering media, the back-scattered sample light $\mathbf{E_S}$ forms a speckle field. In this section, we will consider the case where there are N_{speckle} speckles incident on the detector, each with area A_{speckle}. In the case of speckle-resolved detection, each speckle is detected by at least one detector element. As we shall see, this allows us to incoherently combine the information from each speckle and provides an SNR advantage N_{speckle}; that is,

$$\text{SNR}_{\text{speckle-resolved}} \propto N_{\text{speckle}} \times \text{SNR}_{\text{non-speckle-resolved}}. \tag{3}$$

In interferometric techniques, the detected signal can be generally written as

$$I_{\text{det}} = |\mathbf{E_R} + \mathbf{E_S}|^2 = I_R + I_S + \mathbf{E_R}\mathbf{E_S^*} + \mathbf{E_R^*}\mathbf{E_S}. \tag{4}$$

where the reference beam is a plane wave. For this section, we consider the case of shot-noise-limited detection, where $\sigma^2_{\text{noise}} \approx \sigma^2_{\text{shot}}$. Since $I_R \gg I_S$, shot noise is dominated by contributions from the reference arm. In the scenario where there is no scattering media and the target is an ideal mirror reflector, the SNR is of the form

$$\text{SNR}_{\text{ideal}} \propto \eta I_S A_{\text{det}} T. \tag{5}$$

When the detected sample light consists of multiply scattered light, and the sample light forms a speckle field, the signal from a single speckle grain is of the form

$$I_{\text{sig},i} = E_R \mathbf{E_{S,i}} = E_R E_{S,i} e^{j\theta_{s,i}}, \tag{6}$$

Biomedical Optics EXPRESS

where $E_{s,i}$ and $\theta_{s,i}$ is the amplitude and phase of the i^{th} speckle grain. The SNR of such a system depends on how the total sample signal is detected. We consider the case where there are N_{speckle} speckle grains incident on the detector, each with area A_{speckle}.

3.2.1. Speckle-resolved detection

In the case of speckle-resolved detection, each speckle is detected by at least one detector element, and the total signal can be found by summing the magnitude of each speckle. This results in the following expected signal:

$$\mathbb{E}\left[\sum_{i=1}^{N_{\text{speckle}}} A_{\text{speckle}} E_R E_{S,i}\right] = A_{\text{speckle}} E_R N_{\text{speckle}} \mathbb{E}[E_S]. \tag{7}$$

The shot noise of each speckle is $\sigma^2_{shot,i} = I_R A_{\text{speckle}} \eta T$. Since the shot noise of each speckle is uncorrelated, the shot noise of the summed signal is $\sigma^2_{shot} = N_{\text{speckle}} \sigma^2_{shot,i} = I_R A_{\text{speckle}} N_{\text{speckle}} \eta T$.

The SNR is

$$\text{SNR}_{\text{speckle-resolved}} \propto \frac{(\eta T A_{\text{speckle}} N_{\text{speckle}} E_R \mathbb{E}[E_S])^2}{\eta T A_{\text{speckle}} I_R N_{\text{speckle}}} = \eta T N_{\text{speckle}} P_{\text{speckle}}, \tag{8}$$

where $I_S = \mathbb{E}[E_S]^2$ and $P_{\text{speckle}} = I_S A_{\text{speckle}}$. The SNR scales linearly with N_{speckle} and is directly proportional to the total number of photo-electrons detected from the sample.

3.2.2. Non-speckle-resolved detection

In the case of non-speckle-resolved detection, all of the speckles are incident on a single detector, which integrates the signal. Therefore, the detected intensity and signal follow:

$$I_{\text{det}} = \sum_{i=1}^{N_{\text{speckle}}} |\mathbf{E_R} + \mathbf{E_{S,i}}|^2 = \sum_{i=1}^{N_{\text{speckle}}} \left[I_R + I_{S,i} + \mathbf{E_R E^*_{S,i}} + \mathbf{E^*_R E_{S,i}}\right] \tag{9}$$

$$I_{\text{sig}} = E_R \sum_{i=1}^{N_{\text{speckle}}} E_{S,i} e^{j\theta_{s,i}} \tag{10}$$

The expected value of the signal is

$$\mathbb{E}\left[\left|E_R \sum_{i=1}^{N_{\text{speckle}}} E_{S,i} e^{j\theta_{s,i}}\right|\right] = E_R \sqrt{N_{\text{speckle}}}\, \mathbb{E}\left[E_S\right] \tag{11}$$

The shot noise is still dominated by contributions from the reference beam and is $\sigma^2_{shot} = A_{\text{speckle}} N_{\text{speckle}} I_R \eta T$. Therefore, the SNR is:

$$\text{SNR}_{\text{non-speckle-resolved}} \propto \frac{\left(A_{\text{speckle}} E_R \sqrt{N_{\text{speckle}}}\, \mathbb{E}\left[E_S\right] \eta T\right)^2}{A_{\text{speckle}} N_{\text{speckle}} \eta T I_R} = \eta T P_{\text{speckle}} \tag{12}$$

Unlike the case of speckle-resolved detection, the SNR is proportional to the average number of photo-electrons detected in a single speckle.

3.2.3. Impact of averaging multiple acquired signals

In order to boost the SNR, one can acquire and incoherently average multiple signal traces. In this case, the signal term remains unchanged but the noise term decreases by a factor of N_{ave}. Thus, $\text{SNR}_{N_{\text{ave}}} = N_{\text{ave}} \text{SNR}_{\text{single}}$.

Biomedical Optics EXPRESS

3.2.4. SNR comparison

Speckle resolution provides an SNR advantage of N_{speckle} as it allows us to incoherently combine the power from each speckle and measure the total back-scattered power from the sample. In contrast, in the non-speckle-resolved scenario, the measured signal is proportional to the photons contained within a single speckle. In essence, speckle resolution allows us to incoherently average the information from multiple speckles in a single-shot manner.

To highlight the impact of speckle-resolved detection, we compared it to non-speckle-resolved detection and conventional OCT. B-scans were acquired with the detection and illumination focused on the target in order to simulate conventional OCT acquisition. 4 different thicknesses of the $g = 0.91$ phantom were imaged: $t = 1.06, 1.25, 1.45$ and 2.12mm. After detecting the interference image, spatio-angular filtering was applied to the conventional OCT case to mimic confocal detection. The same data set was also processed in a non-speckle-resolved manner. For a chrome target placed 1.25 mm behind a $g = 0.91$ scattering phantom, the chrome signal is clearly resolved in the speckle-resolved case, in contrast to conventional OCT processing and non-speckle-resolved detection (Fig. 7(a)). Similar results were seen for the $t = 1.45, 2.12$mm phantoms.

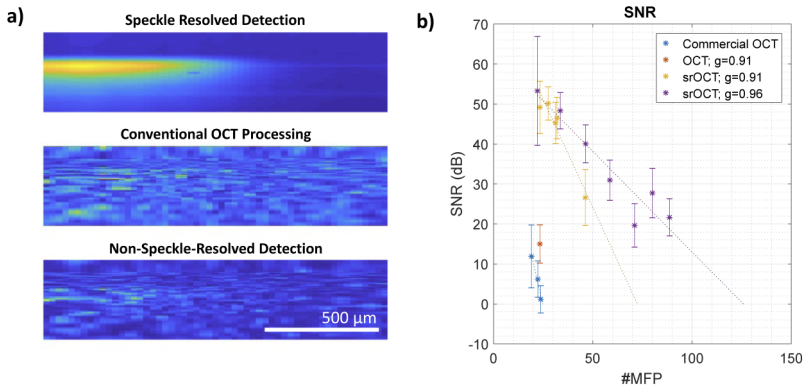

Fig. 7. SNR Advantage of Speckle Resolution. a) B-scans of data processed using speckle-resolved detection, conventional OCT processing, and non-speckle-resolved detection highlight the SNR advantage to speckle-resolved detection. A chrome target was placed behind 1.25mm of g=0.91 scattering phantom. b) SNR for Speckle-Resolved, Non-Speckle-Resoled, and Conventional OCT for different scattering media thicknesses. The results from using a commercial OCT system are also presented.

We measured the SNR of srOCT a-scans acquired of the chrome target through the scattering phantoms. We also imaged the 1 µm-bead phantoms with a commercial OCT system (Ganymede 611C1 Spectral-Domain OCT; Thorlabs, NJ). According to Mie theory, the scattering properties of the phantom was $\mu_S = 9\text{mm}^{-1}$ and $g = 0.89$ at $\lambda = 930$nm. The SNR of the commercial OCT, OCT processing, and srOCT has been provided in Fig. 7. Both the conventional OCT processing and commercial OCT systems appear to have similar SNR. The data from the srOCT system has approximately 40 dB improvement in SNR over conventional OCT processing.

3.3. Biological results

We lastly demonstrated srOCT on a biological sample (Fig. 8). We first measured the resolution through chicken breast tissue (Fig. 8(a)). A piece of chicken breast tissue was sandwiched in between a coverglass and a USAF resolution target, with the square target (approximate location shown in green) used to estimate the resolution. The tissue thickness was controlled using iSpacers (Sunjin Lab, Taiwan). Cross-sectional b-scans of the target acquired through

Biomedical Optics EXPRESS

two thicknesses of chicken tissue have been shown in Fig. 8(a),ii. When imaging underneath chicken breast tissue, the axial and lateral resolution steadily worsened with increasing thickness (Fig. 8(a),iii); however, even at a depth of 4.4 mm, a resolution of approximately 400 µm was achieved.

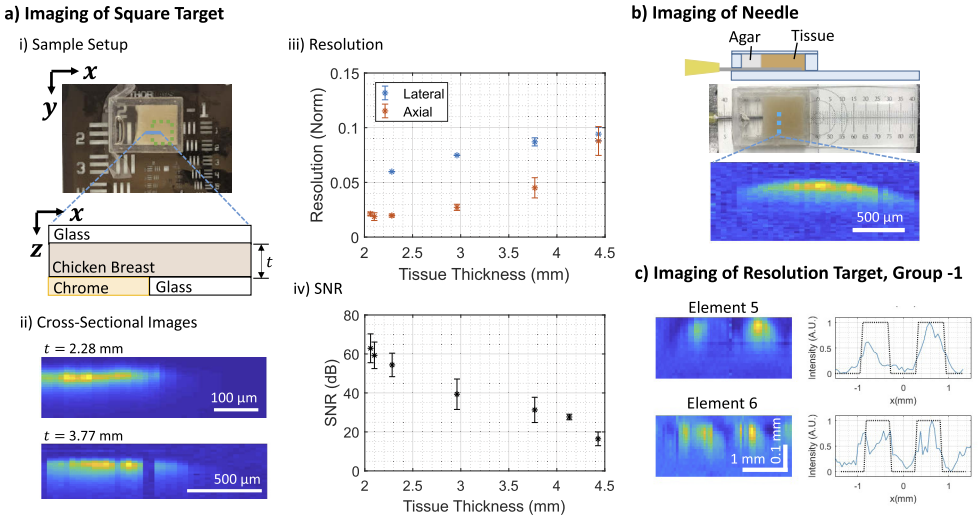

Fig. 8. srOCT Imaging through Chicken Breast Tissue. a) A USAF resolution target was used to determine the resolution and SNR. i) A piece of chicken breast tissue was sandwiched between a coverslip and the target and covers a clear square pattern (approximate location in green). ii) Cross-sectional images of the target, acquired underneath chicken tissue thicknesses of t = 2.28, 3.77mm. iii) The lateral and axial resolution of srOCT through various chicken tissue thicknesses. iv) The measured SNR. e) A 20G needle was placed underneath 4.1 mm chicken tissue. Pictorial schematic and photo of setup is provided along with a cross-sectional image acquired using srOCT. The blue dashed line shows the approximate location of the cross-sectional image. f) Cross-sectional images of Group −1, Elements 4 – 6 of a USAF target located underneath 3.8 mm of tissue, along with their corresponding line plot. The dashed lines show the approximate location of the bars.

Figure 8(b,c) provide images of a needle and USAF target, respectively, that are buried under chicken breast tissue. Although not visible by eye, we can clearly resolve the top of the needle located under 4.1 mm of chicken breast tissue using srOCT. In the case of the USAF target located underneath 3.8 mm of tissue, the depth and lateral position of the bars are clearly distinguished (Fig. 8(c)). The plots on the right show the srOCT response (in blue) along with the theoretical location of the bars (in dashed lines).

4. Discussion

In summary, we present Speckle-Resolved OCT (srOCT), a new method that preferentially detects weakly scattered photons in a speckle-resolved manner to enable imaging past the ballistic limit at moderate resolution. Spatio-angular filtering was employed to preferentially reject the diffusely scattered photons. Using this method, we were able to image up to 47 MFPs in g = 0.91 scattering media, 89 MFPs in g = 0.96 scattering media, and 4.4 mm depth in chicken breast tissue at sub-millimeter resolution. Since srOCT relies on the preferential detection of weakly scattered photons, srOCT does not require intensive computational modelling and reconstruction in order to recover the sample information. Instead, srOCT is able to acquire depth-resolved images of the sample by directly measuring the back-scattered sample intensity from a given

Biomedical Optics EXPRESS

location. In the remainder of this section, we discuss the results of our investigations as well as some factors that impact system performance.

We demonstrate that speckle-resolved detection is an efficient method to detect the back-scattered light from the sample as $\mathrm{SNR}_{\text{speckle-resolved}} \propto N_{\text{speckle}} P_{\text{speckle}}$. In contrast, $\mathrm{SNR}_{\text{non-speckle-resolved}} \propto P_{\text{speckle}}$. Without speckle-resolved detection, one would need to either increase the exposure time by N_{speckle} times or acquire N_{speckle} data points and average them in order to achieve the same SNR boost. For our proof-of-concept system, each image, which yielded a measure of the sample intensity at one x, y, z point in the sample, was acquired with an exposure time of 1 ms to 4 ms. $N_{\text{speckle}} =\sim 4\times10^5$ speckles. In order to achieve the same SNR boost with the conventional non-speckle-resolved detection scheme, one would need to increase the imaging time by $\sim \times10^5$ times; that is, it would take $10^2 \sim 10^3$ sec to measure the back-scattered sample intensity at one point in the sample. In practice, N_{speckle} is limited by the number of detector elements. Since many cameras have $10^5 \sim 10^6$ pixels, speckle-resolved detection can provide a large boost in SNR in a single-shot manner, making it more suitable for imaging dynamic samples.

Experimentally, our proof-of-concept system took approximately 2 mins to acquire a 40 pixel x 40 pixel b-scan image. This acquisition time was limite by the actuators that were used to perform the axial and lateral scanning, as 50 ms delays were added to provide sufficient time for the motors to settle into their new position. Each interference pattern image, which provided a measure of the intensity at one pixel in the processed b-scan, was acquired with an exposure time ranging from 1 to 4 ms. Thus, the acquisition time can be shortened with better optimization of the hardware used for scanning.

We also investigated the impact of spatio-angular filtering on imaging resolution and found that spatio-angular filtering improved resolution in simulation, but the improvement was modest in experiments. One reason is that the ranges of spatial and angular restrictions tested were much wider in simulation than experimentally. The ranges used in simulation were $r_{thr} \in [0.25\text{mm}, 100\text{mm}]$ and $\theta_{thr} \in [10\,\text{deg}, 90\,\text{deg}]$ whereas the experimental ranges were $r_{thr,exp} \in [1\ \mu\text{m}, 350\ \mu\text{m}]$ and $\theta_{thr,exp} \in [1\,\text{deg}, 17.4\,\text{deg}]$. In simulation, we saw that changing r_{thr} from 100 mm to 1 mm provided a large improvement in resolution; however, further restriction from 1 mm down to 0.25 mm provided a more modest amount. Since experimentally $r_{thr,exp} \leq 350\ \mu\text{m}$, we expect a smaller enhancement in resolution. The impact of smaller r_{thr} and θ_{thr} were not tested in simulation due to the limited number of photons simulated, but is an interesting avenue to explore in future work.

A second reason for the modest resolution improvement experimentally was because spatio-angular filtering decreased the SNR. Angular filtering increases the speckle size whereas spatial filtering decreases the field-of-view. The net effect is that both spatial filtering and angular filtering reduces the number of detected speckles $N_{speckles}$. This reduction directly impacts the SNR since $\mathrm{SNR}_{\text{speckle-resolved}} \propto N_{\text{speckle}}$. The reduction in SNR limited the amount of restriction that could be applied post-processing and still yield a signal with sufficient SNR to measure the resolution.

Experimentally, the lateral and axial resolutions were quantified by imaging two scattering phantoms with 2 different scattering anisotropies: $g = 0.91$ and $g = 0.96$. We found that, when plotted as a function of MFP, resolution worsened more slowly in the case of imaging through media with higher anisotropy. This makes sense as photons would be more forward scattered in higher anisotropy media, and therefore provide better resolution. Surprisingly, when plotted as a function of TMFPs, both the axial and lateral resolutions for both types of scattering phantoms seem to have more similar trends. Similar to a recently published work, these results suggest that the resolution might be comparable for scattering media with different scattering anisotropies, when the resolution is compared to TMFPs [29]. Further studies are needed to conclusively determine how the scattering strength μ_S and anisotropy g impacts resolution.

Biomedical Optics EXPRESS

Overall, we found that spatial filtering was effective in improving resolution and that angular filtering was only effective when applied in conjunction with spatial filtering. Interestingly, the simulation results suggest that spatial filtering alone without any angular filtering improved imaging resolution. Since the speckle field that is back-scattered from the sample also has a limited spatial extent ($r_{\text{speckle-field}}$), one should design the imaging system with $r_{thr} \leq r_{\text{speckle-field}}$. As spatial filtering has more of an impact on resolution, to improve both the SNR and resolution, one should set r_{thr} first and then set θ_{thr} correspondingly in order to maximize the number of speckles captured by the detection system.

Lastly, our system was designed as a proof-of-concept system to investigate the impact of spatio-angular filtering on imaging resolution and introduce speckle-resolved detection as an efficient means of coherently detecting multiply scattered light. To this end, we designed the detection path to be (1) parallel to the incident light beam and (2) conjugated to the surface of the scattering media. However, srOCT can also be applied to other imaging geometries. Offset illumination and detection can allow for more sensitivity to snake photons by reducing the contribution of sub-surface-scattered photons and surface reflections [13,18,30]. Distinct illumination and detection pathways would also remove issues stemming from reflections off the surface of the sample, other optical components, or objective lens. In our proof-of-concept system, these surface and system reflections hampered our ability to detect the light from the sample as they were orders-of-magnitude larger than the desired sample light.

5. Conclusion

In conclusion, we demonstrated depth-resolved imaging past the ballistic regime by preferentially detecting snake photons in a coherent and speckle-resolved manner. The back-scattered light from the sample was filtered by exit position and exit angle to preferentially detect the weakly-scattered snake photons that provide more imaging resolution. Speckle-resolved detection also allowed for coherent detection of the back-scattered light with high sensitivity. The focus of this paper was to investigate the impact of spatio-angular filtering and introduce the advantage of speckle-resolved detection. To this end, we built a proof-of-concept device, with which we demonstrated imaging through scattering phantoms at a depth that was approximately 3x thicker than the OCT limit. With appropriate optimizations, this project opens up potential for use in applications involving imaging targets deep within scattering media where moderate resolution on the order of hundreds of microns is satisfactory, such as imaging and locating subcutaneous veins for phlebotomy and sclerotherapy [31].

Funding. Natural Sciences and Engineering Research Council of Canada (PGSD); Kernel LLC.

Acknowledgments. The authors would like to thank Dr. Jian Xu, Dr. Haowen Ruan, and Ruizhi Cao for helpful suggestions and feedback.

Disclosures. The authors declare no conflicts of interest.

Data availability. Data underlying the results presented in this paper are not publicly available at this time but may be obtained from the authors upon reasonable request.

References

1. D. Huang, E. A. Swanson, C. P. Lin, J. S. Schuman, W. G. Stinson, W. Chang, M. R. Hee, T. Flotte, K. Gregory, C. A. Puliafito, and J. G. Fujimoto, "Optical coherence tomography," Science **254**(5035), 1178–1181 (1991).
2. S. Kang, S. Jeong, W. Choi, H. Ko, T. D. Yang, J. H. Joo, J.-S. Lee, Y.-S. Lim, Q.-H. Park, and W. Choi, "Imaging deep within a scattering medium using collective accumulation of single-scattered waves," Nat. Photonics **9**(4), 253–258 (2015).
3. M. Kempe, A. Genack, W. Rudolph, and P. Dorn, "Ballistic and diffuse light detection in confocal and heterodyne imaging systems," J. Opt. Soc. Am. A **14**(1), 216–223 (1997).
4. A. Badon, A. C. Boccara, G. Lerosey, M. Fink, and A. Aubry, "Multiple scattering limit in optical microscopy," Opt. Express **25**(23), 28914–28934 (2017).
5. M. A. Choma, M. V. Sarunic, C. Yang, and J. A. Izatt, "Sensitivity advantage of swept source and Fourier domain optical coherence tomography," Opt. Express **11**(18), 2183–2189 (2003).

Biomedical Optics EXPRESS

6. Z. Yaqoob, J. Wu, and C. Yang, "Spectral domain optical coherence tomography: a better OCT imaging strategy," BioTechniques **39**(6S), S6–S13 (2005).
7. D. A. Boas, D. H. Brooks, E. L. Miller, C. A. DiMarzio, M. Kilmer, R. J. Gaudette, and Q. Zhang, "Imaging the body with diffuse optical tomography," IEEE Signal Process. Mag. **18**(6), 57–75 (2001).
8. Y. Hoshi and Y. Yamada, "Overview of diffuse optical tomography and its clinical applications," J. Biomed. Opt. **21**(9), 091312 (2016).
9. E. M. Hillman, D. A. Boas, A. M. Dale, and A. K. Dunn, "Laminar optical tomography: demonstration of millimeter-scale depth-resolved imaging in turbid media," Opt. Lett. **29**(14), 1650–1652 (2004).
10. L. V. Wang and H.-I. Wu, *Biomedical Optics: Principles and Imaging* (John Wiley & Sons, 2012).
11. A. Wax and J. Thomas, "Measurement of smoothed Wigner phase-space distributions for small-angle scattering in a turbid medium," J. Opt. Soc. Am. A **15**(7), 1896–1908 (1998).
12. R. K. Wang, "Signal degradation by multiple scattering in optical coherence tomography of dense tissue: a Monte Carlo study towards optical clearing of biotissues," Phys. Med. Biol. **47**(13), 2281–2299 (2002).
13. M. G. Giacomelli and A. Wax, "Imaging beyond the ballistic limit in coherence imaging using multiply scattered light," Opt. Express **19**(5), 4268–4279 (2011).
14. Y. Chen, H. Chen, D. Dilworth, E. Leith, J. Lopez, M. Shih, P.-C. Sun, and G. Vossler, "Evaluation of holographic methods for imaging through biological tissue," Appl. Opt. **32**(23), 4330–4336 (1993).
15. P. Naulleau and D. Dilworth, "Holographic first-arriving-light signal-to-noise ratio enhancement by differential holography," Opt. Lett. **20**(22), 2354–2356 (1995).
16. E. N. Leith, K. D. Mills, S. Grannell, D. S. Dilworth, B. D. Athey, and J. Lopez, "Analysis of time-gated imaging through scattering media by a Fourier optics approach," J. Opt. Soc. Am. A **19**(3), 532–536 (2002).
17. T. E. Matthews, M. G. Giacomelli, W. J. Brown, and A. Wax, "Fourier domain multispectral multiple scattering low coherence interferometry," Appl. Opt. **52**(34), 8220–8228 (2013).
18. Y. Zhao, J. R. Maher, M. M. Ibrahim, J. S. Chien, H. Levinson, and A. Wax, "Deep imaging of absorption and scattering features by multispectral multiple scattering low coherence interferometry," Biomed. Opt. Express **7**(10), 3916–3926 (2016).
19. T. E. Matthews, M. Medina, J. R. Maher, H. Levinson, W. J. Brown, and A. Wax, "Deep tissue imaging using spectroscopic analysis of multiply scattered light," Optica **1**(2), 105–111 (2014).
20. Q. Fang and D. A. Boas, "Monte Carlo simulation of photon migration in 3d turbid media accelerated by graphics processing units," Opt. Express **17**(22), 20178–20190 (2009).
21. E. N. Leith and J. Upatnieks, "Reconstructed wavefronts and communication theory," J. Opt. Soc. Am. **52**(10), 1123–1130 (1962).
22. E. N. Leith and J. Upatnieks, "Wavefront reconstruction with continuous-tone objects," J. Opt. Soc. Am. **53**(12), 1377–1381 (1963).
23. U. Schnars and W. Jüptner, "Direct recording of holograms by a CCD target and numerical reconstruction," Appl. Opt. **33**(2), 179–181 (1994).
24. E. Cuche, P. Marquet, and C. Depeursinge, "Simultaneous amplitude-contrast and quantitative phase-contrast microscopy by numerical reconstruction of Fresnel off-axis holograms," Appl. Opt. **38**(34), 6994–7001 (1999).
25. Z. Yaqoob, T. Yamauchi, W. Choi, D. Fu, R. R. Dasari, and M. S. Feld, "Single-shot full-field reflection phase microscopy," Opt. Express **19**(8), 7587–7595 (2011).
26. A. Maznev, T. Crimmins, and K. Nelson, "How to make femtosecond pulses overlap," Opt. Lett. **23**(17), 1378–1380 (1998).
27. S. Witte, A. Plauşka, M. C. Ridder, L. van Berge, H. D. Mansvelder, and M. L. Groot, "Short-coherence off-axis holographic phase microscopy of live cell dynamics," Biomed. Opt. Express **3**(9), 2184–2189 (2012).
28. J. W. Goodman, *Speckle Phenomena in Optics: Theory and Applications* (Roberts and Company Publishers, 2007).
29. E. T. Jelly, Y. Zhao, K. K. Chu, H. Price, M. Crose, Z. A. Steelman, and A. Wax, "Deep imaging with 1.3 μm dual-axis optical coherence tomography and an enhanced depth of focus," Biomed. Opt. Express **12**(12), 7689–7702 (2021).
30. Y. Zhao, K. K. Chu, E. T. Jelly, and A. Wax, "Origin of improved depth penetration in dual-axis optical coherence tomography: a Monte Carlo study," J. Biophotonics **12**(6), e201800383 (2019).
31. C.-T. Pan, M. D. Francisco, C.-K. Yen, S.-Y. Wang, and Y.-L. Shiue, "Vein pattern locating technology for cannulation: A review of the low-cost vein finder prototypes utilizing near infrared (NIR) light to improve peripheral subcutaneous vein selection for phlebotomy," Sensors **19**(16), 3573 (2019).